

Reflectance properties of the Acktar Magic Black™ coating for the radiation near the Lyman- α line of hydrogen: measurements and phenomenological model of the BRDF

Marek Strumik^{Ⓢ, a, *} Martyna Wardzińska^{Ⓢ, b} Maciej Bzowski^{Ⓢ, a}
Przemysław Wachulak^{Ⓢ, b} Roman Wawrzaszek^{Ⓢ, a} Tomasz Fok^{Ⓢ, b} Andrzej Bartnik^{Ⓢ, b}
Karol Mostowy^{Ⓢ, a} Henryk Fiedorowicz^{Ⓢ, b} Łukasz Węgrzyński^{Ⓢ, b}
and Mateusz Majszyk^{Ⓢ, b}

^aSpace Research Centre PAS (CBK PAN), Warsaw, Poland

^bMilitary University of Technology, Institute of Optoelectronics, Warsaw, Poland

ABSTRACT. Optical surfaces of space instruments usually need to be blackened to minimize adverse effects affecting their performance in photometric, spectrometric, and imaging applications. Blackening is often obtained by application of coatings that strongly absorb the incoming photon flux and diffusively scatter the incident photons. We discuss reflectance measurements and a phenomenological model of the bidirectional reflectance distribution function (BRDF) for the Magic Black™ coating, which is a commercial product supplied by the Acktar company. The coating has a vast satellite-instrument heritage and is planned to be used in the GLOWS photometer onboard the upcoming NASA Interstellar Mapping and Acceleration Probe mission. The reflectance measurements were conducted at ~ 121.6 nm, corresponding to the Lyman- α line for hydrogen, which is important in astrophysics. This line is commonly considered a crossover between the far ultraviolet and extreme ultraviolet spectral ranges. To generate radiation in this range, a laser-plasma source based on the gas-puff target was used. Six samples coated with Acktar Magic Black™ were studied in an optical system with a back-illuminated CCD camera as a detector. The measurements were used to derive the phenomenological BRDF model based on a series of analytic fits to the measurements, which makes it easily applicable in both numerical simulations and manual calculations. The formulas provide an approximation in the full hemispheric domain, i.e., both for the in-specular-plane and out-of-specular-plane behaviors of the BRDF for the coating. A similar fit-based phenomenological model is also described for the visible range (the wavelength of 532 nm) as a byproduct of our analysis for the UV range.

© The Authors. Published by SPIE under a Creative Commons Attribution 4.0 International License. Distribution or reproduction of this work in whole or in part requires full attribution of the original publication, including its DOI. [DOI: [10.1117/1.JATIS.10.1.018004](https://doi.org/10.1117/1.JATIS.10.1.018004)]

Keywords: reflectance; coatings; far ultraviolet; extreme ultraviolet; laser-plasma source; Lyman- α

Paper 23131G received Oct. 27, 2023; revised Jan. 19, 2024; accepted Jan. 22, 2024; published Feb. 8, 2024.

1 Introduction

Black coatings are widely used for improving the performance of optical instruments, for example, to minimize internal reflections in the optical paths. Accurate characterization of

*Address all correspondence to Marek Strumik, maro@cbk.waw.pl

coatings at the transition between the far ultraviolet (FUV) and extreme ultraviolet (EUV) regimes is crucial for a wide range of applications, including lithography¹ and spectroscopy² among others. Space instruments designed for application in solar and heliospheric physics require a highly absorptive coating to suppress the stray light. In particular, collimators that subtend the desired field of view of optical instruments are required to suppress stray light effectively.

The Space Research Center PAS (CBK PAN) is preparing a GLOWS (GLObal Solar Wind Structure) photometer for the NASA's Interstellar Mapping and Acceleration Probe (IMAP) space mission.³ The GLOWS photometer will measure the intensity of the heliospheric back-scatter glow, which is generated by resonant scattering of solar Lyman- α (121.6 nm) photons on interstellar neutral hydrogen (ISN H) atoms penetrating the heliosphere. The GLOWS measurements will enable investigation of the helio-latitudinal structure of the solar wind and radiation pressure acting on ISN H.⁴ To fulfill the mission's requirements, the instrument must meet stringent stray-light-suppression requirements, which are achieved by a suitable optical design and blackening its optical baffle and collimator surfaces with the Acktar Magic Black™ coating.⁵

The Acktar Magic Black™ is a coating from an entire family of black coatings offered by the Acktar company, which are characterized by a low reflectance in a broad temperature range in a wide range of wavelengths. These properties make the coatings interesting in space-physics and astronomical contexts for applications in spaceborne instruments. Besides the IMAP/GLOWS instrument mentioned above, past or future missions that use the Acktar black coatings include, among others, Solar Orbiter/METIS,⁶ CHEOPS,⁷ Sentinel-4/UVN,⁷ ULTRASAT,⁸ James Webb Space Telescope,⁹ and JUICE.¹⁰

Development of an instrument requires a number of numerical simulations, for which the reflectance properties of the coating need to be known. Reflectance measurements are conventionally converted into the bidirectional reflectance distribution function (BRDF), which provides a rigorous description of reflectance properties as a function of the incidence and scattering/reflection directions. In the literature available to date and in the materials provided by the manufacturer, one can find a relatively complete set of scatterometer measurements of the Acktar Magic Black™ coating for selected wavelengths in the visible range (VIS).^{6,7} However, for the UV range, there are available only measurements of the BRDF for 193 nm in the specular plane and of the reflectance for a limited set of the incidence and scattering angles for ~ 13 nm.¹¹ Lyman- α diffuse-reflectance characteristics of 10 different materials were discussed in Ref. 12. This study includes the Acktar's Spectral Black™ adhesive foil, some carbon-nanotube, and carbon-foam coatings, and Laser Black coating manufactured by the Epner Company. The measurements were performed for near-normal incidence and selected scattering angles. Relatively little data on the reflectance of coatings in the UV range, including specifically measurements for ~ 121.6 nm, seem to be due to difficulties specific to the FUV and EUV regimes (measurements in vacuum, need for a special type of radiation sources and detectors, calibration issues, etc.). The goal of this paper is to address this gap by measuring the reflectance and developing a phenomenological model of the BRDF for ~ 121.6 nm in the full scattering hemisphere.

The measurements of the reflectance of Acktar Magic Black™ samples discussed in this paper were performed at the Institute of Optoelectronics of the Military University of Technology in Warsaw. Radiation in the EUV and FUV ranges¹³ was produced with a laser plasma radiation source based on a double-stream gas puff target.¹⁴ Due to difficulties specific to the FUV and EUV regimes, the measurements do not cover the entire hemisphere but characterize comprehensively certain parts, including quasi-perpendicular (relative to the sample surface) and quasi-parallel cases. This set of measurements is shown to properly constrain the parameters of the BRDF model proposed in this paper.

The phenomenological BRDF model is based on a series of analytic fits to the measurements discussed above. To obtain the BRDF model for ~ 121.6 nm, in the first step, we develop a methodology and pre-validate it using measurement data available in the literature for the VIS, thus a BRDF model for 532 nm is also discussed here as a byproduct of our analysis. The methodology discussed in this paper is more general and can be used also to construct BRDF models for other wavelengths provided that appropriate measurement data are available.

This paper is organized as follows. Section 2 describes the experimental setup and Sec. 3 discusses the obtained raw reflectance measurements. The methodology for the phenomenological model of the BRDF is presented in Sec. 4. The BRDF models for ~ 532 and ~ 121.6 nm are derived in Sec. 5. Numerical simulations using our BRDF model are discussed in Sec. 6 to show that they reproduce the original reflectance measurements. Section 7 contains a general discussion of the obtained results and conclusions.

2 Experimental Setup

The measurements were performed for flat aluminum surfaces covered with the Acktar Black coating. The measurements were taken at various incidence angles θ_i (measured from the normal to the sample) to obtain on-axis—specular reflectance, as well as off-specular reflectance, where the scattering angle θ_s is $\delta = \pm 15$ deg around the specular direction. Two series of measurements were performed. Series I (specular reflectance) is summarized in Sec. 3.1, where $\theta_i = [18, 45, 75, 80]$ deg, and series II (off-specular reflectance) is presented in Sec. 3.2, where $\theta_i = [45, 75, 80]$ deg.

For the reflectance measurements, an experimental setup presented in Fig. 1 was developed, consisting of a laser plasma source, three baffles with diameters of 4.8, 16, and 4.63 mm, and a back-illuminated CCD camera (DX420-BN Andor, Oxford Instruments), cooled down to a temperature of -20°C , with a narrowband VUV/UV optical filter¹⁵ (Acton FN122-XN-1D), hereafter called Lyman- α filter, mounted to transmit the radiation within a narrow wavelength range around the hydrogen line (121.6 nm). The camera's chip size was 1024×256 pixels, the pixel size was $26 \times 26 \mu\text{m}^2$, and the exposure time 5 s. The distance z between the source and the sample was in the range of 346 to 360 mm, depending on the series of measurements. The distance between the source and the CCD camera was 0.486 to 0.5 m, keeping in mind to always have the source–camera distance constant during the reference and angular measurements. 1.

To produce EUV radiation, we used a laser-plasma radiation source based on a double stream Xe/He gas puff target.¹⁶ The source was driven by a Nd:YAG laser system (NL129 EKSPILA, Lithuania) with a pulse energy of 6.27 to 6.43 J and a pulse duration of 6.44 to 6.87 ns. These laser impulses were focused with an $f = 100$ mm lens onto a double-stream gas puff target. Two nozzles are required to produce this type of target. The inner nozzle injects a small amount of working gas (xenon) into the vacuum 200 μs after receiving a synchronization

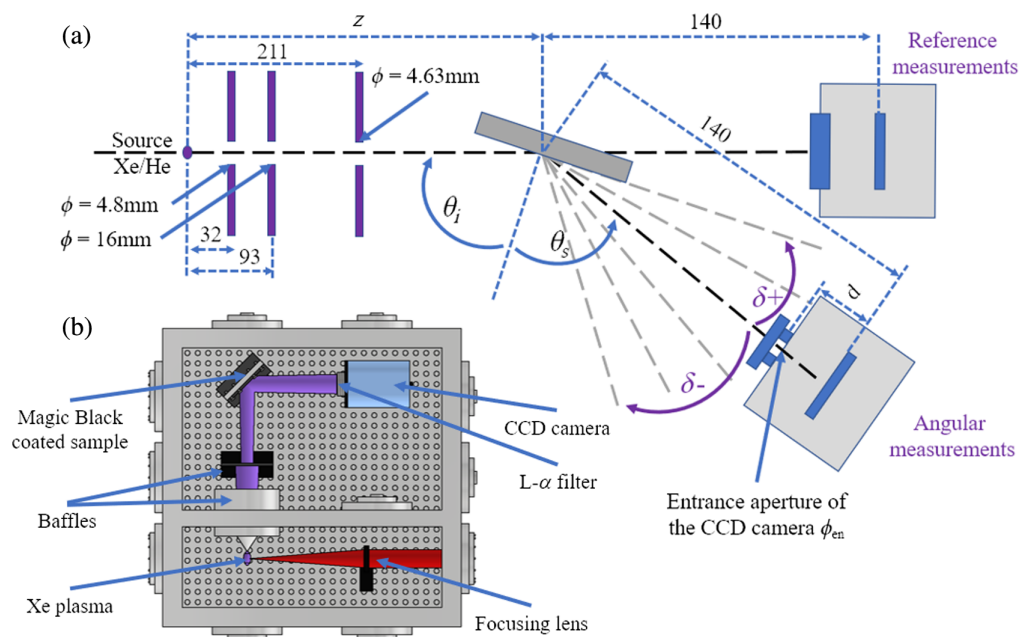


Fig. 1 A scheme of the experimental setup used in reflectance measurements: (a) with dimensions and visualization of the reference and angular measurements and (b) with a description of each component.

pulse from the laser power supply. The nozzle remains open for 750 μs . The second ring-shaped nozzle is designed to inject a low- Z -number gas, in this case it is helium, to increase the density of the working gas by confining it by the radial flow of the He gas. It opens 400 μs after receiving a synchronization pulse and remains open for 555 μs . At 1 ms, after the synchronization pulse, a laser pulse is emitted, which irradiates the Xe/He gas puff target to produce a plasma. This plasma emits efficiently the EUV radiation used in the subsequent reflectance measurements. The gas pressures and nozzle opening and closing times were optimized to provide the best radiation intensity in the wavelength range of interest. Energy fluctuations of the EUV source were estimated as $\sim 9\%$. The data were taken for the Xe plasma, which emits a broadband spectrum, spanning from 1 nm to far infrared. A part of the spectrum measured using a grating spectrometer is shown in Fig. 2(a).

For spectral measurements in the FUV/EUV range, an HP Spectroscopy GmbH (formerly known as DR. HOERLEIN + PARTNER GbR) spectrograph was used. The spectrograph is based on a concave flat-field varied-linespace grating, which has 1200 grooves/mm. The spectral range of this instrument is 40 to 280 nm, and the resolution is 0.1 nm. To narrow down the spectrum, an interference Lyman- α filter was used, mounted at the entrance aperture of the CCD camera, to select only radiation in the range 115 to 135 nm with a spectral peak at ~ 121.1 nm. The measured peak transmission of the Lyman- α filter was $\sim 5\%$. During the measurements of the Lyman- α filter's transmission, a lithium fluoride (LiF) filter was used to cut off the strong impact of higher diffraction orders from shorter wavelengths, which were overlapping the radiation from the spectral range near 100 nm. The thickness of LiF filter was 3 mm. The spectrum of Xe plasma radiation transmitted by the LiF filter is presented in Fig. 2(a)—pink line. The spectrum of Xe plasma radiation transmitted by the LiF and Lyman- α filters is presented in Fig. 2(a)—blue line (Xe spectrum with Lyman- α filter was multiplied by 10). The measured transmission of Lyman- α filter is presented in Fig. 2(b). The optimal EUV photon yield was obtained for the gas pressures equal to 9 bars for xenon and 6 bars for helium.

Three baffles/apertures were used to direct the unfiltered EUV beam toward the sample. The center of the sample was located 346 to 360 mm from the plasma. The sample was mounted on a rotation mount so that the incidence angle θ_i of the EUV beam, measured from the normal direction to the sample surface, could be easily changed in the range from 18 deg to 80 deg. The CCD camera with an entrance aperture, defined by the Lyman- α filter placed in front of the CCD detector, was used as a detector. In both measurement series, between the filter surface and the camera chip, a second aperture was mounted. The diameter of the entrance aperture was 7.2 mm in series I and 7.5 mm in series II, which can be seen as a circular intensity pattern in Fig. 3. The distance between the aperture and the camera's chip was 36.2 mm in series I and 30 mm in series II. The camera's position was manually adjusted to receive either the specularly reflected beam for each incidence angle (so that the angle $\delta = 0$ deg) or the reflected signal for off-specular case ($\delta \neq 0$ deg, see Fig. 1). The distance between the sample's center and the CCD chip was kept

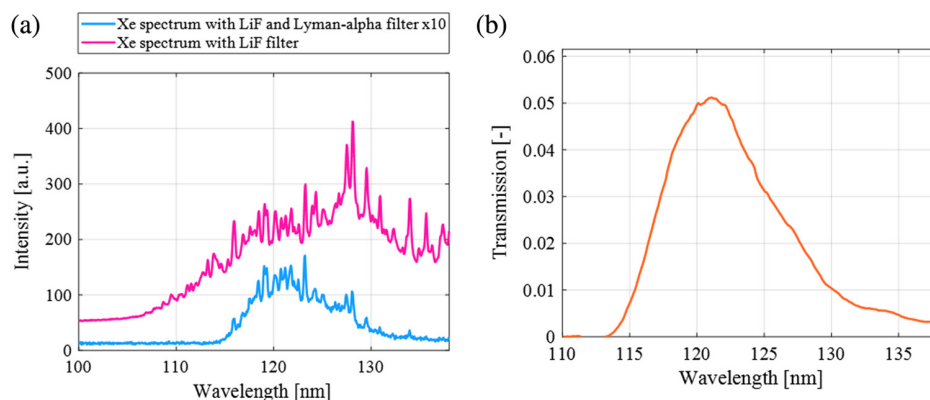


Fig. 2 (a) The comparison of the Xe plasma spectrum measured with the LiF filter (pink line), and the spectrum measured with additional Lyman- α filter (blue line). Note that the Xe plasma spectrum with the Lyman- α filter has been multiplied by 10 to better visualize the difference between both spectra. (b) The transmission of the Lyman- α filter used in the reflectance measurements.

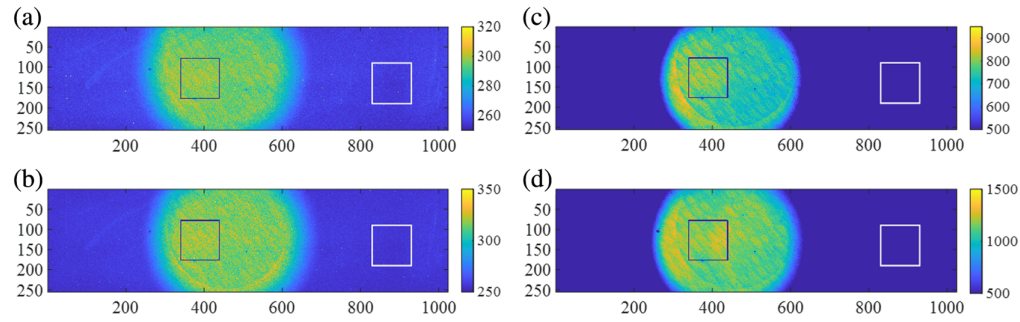


Fig. 3 Reflectance raw data taken for xenon at (a) 18 deg, (b) 45 deg, (c) 75 deg, and (d) 80 deg. Note the intensity change indicated by the colorbar.

constant during the measurements and was equal to 140 mm. The angle θ_s is the scattering angle and for the specular reflection $\theta_i = \theta_s$. For the off-specular reflection $\theta_i \neq \theta_s$, and the scattering angle can be described as

$$\theta_s = \theta_i + \delta, \quad (1)$$

where $\delta = \pm 15$ deg was manually adjusted by moving the CCD camera toward the plane parallel to the sample surface (+) and in the opposite direction (–).

3 Experimental Results

3.1 Specular Reflectance

For the specular reflectance measurements (series I), the reference and reflected signals (hereafter referred to as the angular data) were measured separately. The reference signal was measured without the sample, so the EUV beam illuminated the CCD camera directly, keeping the distance from the plasma to the CCD chip equal to 486 mm, as shown in Fig. 1. Typically, 1 to 10 EUV pulses were integrated in the case of reference measurements, and 30 to 50 EUV pulses were used to measure the reflected signal, depending on the angle of incidence. The variations in the number of pulses are accounted for in the averaged measured reflectances presented in this section.

Measurements were conducted for six flat aluminum samples coated with Acktar Magic Black™. The details of the coating manufacturing process are not known since they are proprietary technology developed by the Acktar company. The samples' size was 1×1 in². According to the manufacturer specification, the coating was performed on top of the aluminum sample and the coating was the same for all measured samples. The measurements discussed in this section were performed only for specular reflection for the incidence and reflection angles of $\theta_i = [18, 45, 75, 80]$ deg. Example images from the CCD camera for several angles are presented in Fig. 3. In each image in Fig. 3, there is an imprint that was caused by CCD's array contamination. The imprint resulted in a decrease in the signal, which was corrected in the post-processing of the measurement data. The angle of 18 deg was the minimal possible angle due to the chamber dimensions and geometry.

Twelve data images were captured as a data series for each angle and each sample. A black square added approximately in the center of each image in Fig. 3 indicates the position of spatial signal integration. The intensity registered by the CCD camera from this region was integrated by summing up all pixel intensities. For each image (including the reference and angular data), the background signal was subtracted. The white-border square area in each image in Fig. 3 shows the region where the background signal was integrated. Both squared regions (with the black and white border) were exactly 100×100 pixels in size. For each data series, the standard deviation σ was calculated, to estimate the error. Dixon's Q -test¹⁷ was used to identify the outliers in a dataset. The test confirmed that with a probability of 99%, there were no outliers during the measurement. The images were averaged to improve the signal-to-noise ratio. The Dixon's Q -test is further described in Sec. 3.3.

For each image, the reflectance (R) was calculated as

$$R = \frac{n_{\text{ref}}(I_{\text{an,signal}} - I_{\text{an,background}})}{n_{\text{an}}(I_{\text{ref,signal}} - I_{\text{ref,background}})}, \quad (2)$$

where n_{ref} is the number of laser impulses used in the reference measurements and n_{an} is the angular measurements. For the reference images, $I_{\text{ref,signal}}$ is the signal integrated in the central square, and $I_{\text{ref,background}}$ is the signal integrated inside the square located on the right side of an image. A similar procedure was used for the angular measurements, $I_{\text{an,signal}}$, and $I_{\text{an,background}}$.

Plots with the results are presented in Fig. 4, and the reflectance values are given in Table 1. The reflectance was estimated as the average of the reflectance values for each sample and will be further used to calculate the BRDF value. The standard deviation was calculated from the error propagation formulas, which will be discussed in Sec. 3.4. The results show that the reflectance of the Acktar samples decreases with the decrease of the incidence angle. This kind of behavior

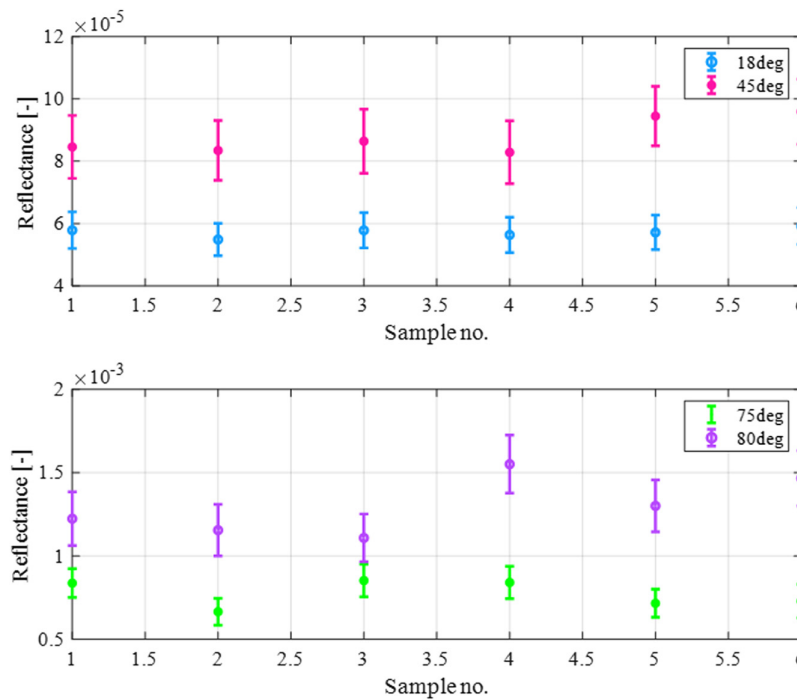


Fig. 4 Raw values of the reflectance for each sample and each angle.

Table 1 Results of the angular measurements for six samples coated with Acktar Magic Black™.

Sample	Reflectance @ 18 deg	Reflectance @ 45 deg	Reflectance @ 75 deg	Reflectance @ 80 deg
1	$(5.79 \pm 0.33) \times 10^{-5}$	$(8.46 \pm 0.57) \times 10^{-5}$	$(8.37 \pm 0.49) \times 10^{-4}$	$(1.22 \pm 0.10) \times 10^{-3}$
2	$(5.49 \pm 0.30) \times 10^{-5}$	$(8.35 \pm 0.54) \times 10^{-5}$	$(6.65 \pm 0.49) \times 10^{-4}$	$(1.15 \pm 0.09) \times 10^{-3}$
3	$(5.78 \pm 0.31) \times 10^{-5}$	$(8.64 \pm 0.59) \times 10^{-5}$	$(8.53 \pm 0.57) \times 10^{-4}$	$(1.11 \pm 0.09) \times 10^{-3}$
	$(5.64 \pm 0.33) \times 10^{-5}$	$(8.29 \pm 0.59) \times 10^{-5}$	$(8.29 \pm 0.56) \times 10^{-4}$	$(1.55 \pm 0.10) \times 10^{-3}$
5	$(5.72 \pm 0.31) \times 10^{-5}$	$(9.45 \pm 0.53) \times 10^{-5}$	$(7.16 \pm 0.48) \times 10^{-4}$	$(1.30 \pm 0.09) \times 10^{-3}$
6	$(5.92 \pm 0.33) \times 10^{-5}$	$(9.59 \pm 0.60) \times 10^{-5}$	$(7.29 \pm 0.58) \times 10^{-4}$	$(1.47 \pm 0.10) \times 10^{-3}$
Mean reflectance	$(5.72 \pm 1.38) \times 10^{-5}$	$(8.80 \pm 2.45) \times 10^{-5}$	$(7.73 \pm 2.24) \times 10^{-4}$	$(1.30 \pm 0.39) \times 10^{-3}$

(low perpendicular reflectance) is desired for tube-like collimators of photometers (i.e., the GLOWS instrument) because it minimizes the transmission of stray light through the instrument.

3.2 Off-Specular Reflectance

The off-specular reflectance measurements (hereafter series II) were performed for a specific incidence angle θ_i while collecting the reflected signal at various angles $\delta \neq 0$ deg from the specular reflection. The size of the samples used was 40×40 mm². The off-axis measurements were performed by moving the CCD camera in the range of (δ) from -15 deg to $+15$ deg from the specular reflection position. Again, at the beginning, the reference data were taken [see Fig. 5(a)]. Next, the data for the angular measurements were obtained. Examples of the data are shown in Figs. 5(b)–5(d).

The results presented in Fig. 6 and Table 2 show that for the incidence angle of 45 deg [Fig. 6(a)], and the reflectance is almost at the same level for each off-specular position. It is more than 10 times smaller in comparison to the results obtained at the position of $\theta_i = 80$ deg. For the high incidence angles of $\theta_i = 75$ deg [Fig. 6(b)] and $\theta_i = 80$ deg [Fig. 6(c)], the reflectance increases with the increase of the scattering angle. For the incidence

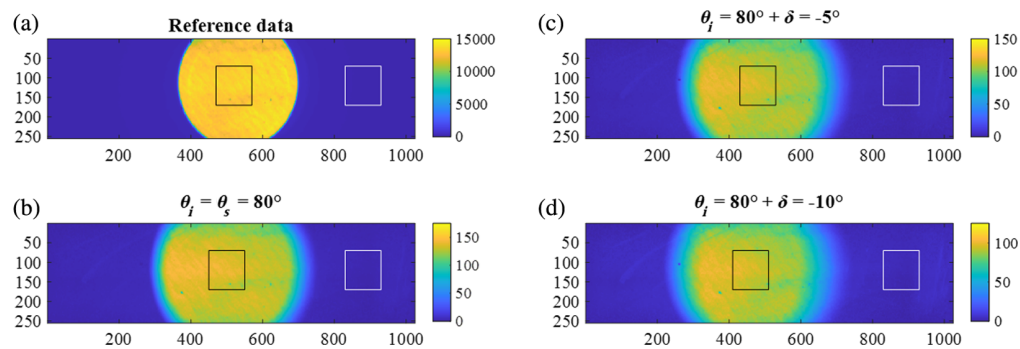


Fig. 5 Reflectance raw data taken for xenon: (a) reference data and (b) examples of the data taken for the incidence angle $\theta_i = 80$ deg for specular reflection, and for off-specular case (c) at $\theta_i = 80$ deg, $\delta = -5$ deg, and (d) at $\theta_i = 80$ deg, $\delta = -10$ deg. Note the intensity change indicated by the colorbar.

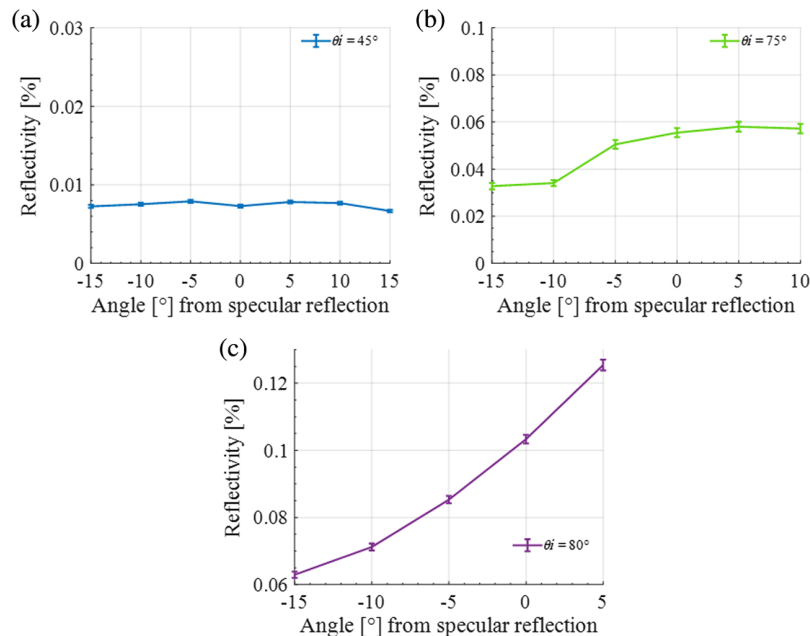


Fig. 6 Results of the off-specular measurements for the incidence angles of (a) $\theta_i = 45$ deg, (b) $\theta_i = 75$ deg, and (c) $\theta_i = 80$ deg.

Table 2 Results of the off-axis measurements for a sample coated with Acktar Magic Black™.

Reflectance [-]		Incidence angle θ_i		
		45 deg	75 deg	80 deg
Angle δ from the specular-reflection direction	-15 deg	$(7.30 \pm 0.38) \times 10^{-5}$	$(3.28 \pm 0.27) \times 10^{-4}$	$(0.62 \pm 0.02) \times 10^{-3}$
	-10 deg	$(7.50 \pm 0.38) \times 10^{-5}$	$(3.41 \pm 0.25) \times 10^{-4}$	$(0.71 \pm 0.02) \times 10^{-3}$
	-5 deg	$(7.90 \pm 0.40) \times 10^{-5}$	$(5.05 \pm 0.37) \times 10^{-4}$	$(0.85 \pm 0.02) \times 10^{-3}$
	0 deg	$(7.30 \pm 0.39) \times 10^{-5}$	$(5.55 \pm 0.38) \times 10^{-4}$	$(1.03 \pm 0.03) \times 10^{-3}$
	5 deg	$(7.80 \pm 0.36) \times 10^{-5}$	$(5.80 \pm 0.41) \times 10^{-4}$	$(1.25 \pm 0.03) \times 10^{-3}$
	10 deg	$(7.70 \pm 0.36) \times 10^{-5}$	$(5.72 \pm 0.40) \times 10^{-4}$	N.A.
	15 deg	$(6.70 \pm 0.28) \times 10^{-5}$	N.A.	N.A.

angle of 75 deg, the number of photons captured by the CCD's array is two times smaller than that for the angle of 80 deg. Moreover, the difference between the highest and smallest results is at a level of $\sim 35\%$. For the incidence angle of 80 deg, the highest reflectance of 0.12% was captured when the camera was moved to $\delta = +5$ deg from specular reflection. A rotation of the CCD camera in the opposite direction causes a nearly linear decrease of the reflectance by $\sim 50\%$. The measurements marked as N.A. were not possible due to the system geometry.

3.3 Q-Dixon's Test for Outliers

During the data pre-processing, the Q -Dixon's test was used to identify the outliers in a dataset consisting of n values. To perform the Q test, the values must be sorted in a non-decreasing sequence. The value of the Q parameter is then determined for the extreme measured values [see Eq. (3) for the minimum value in a dataset and Eq. (4) for the maximum value]:

$$Q_1 = \frac{(x_2 - x_1)}{(x_n - x_1)}, \quad (3)$$

$$Q_n = \frac{(x_n - x_{n-1})}{(x_n - x_1)}. \quad (4)$$

The last step is to read the critical parameter Q_{kr} from the Q -Dixon table and compare it with the obtained value of Q . The test confirmed that with the probability of 99% there were no outliers in the measurement.

3.4 Summary of Raw Reflectance Measurements

The calculated averaged raw reflectance was at the level of $(5.72 \pm 1.38) \times 10^{-5}$ for 18 deg, $(8.80 \pm 2.45) \times 10^{-5}$ for 45 deg, $(7.73 \pm 2.24) \times 10^{-4}$ for 75 deg, and $(1.30 \pm 0.39) \times 10^{-3}$ for 80 deg. The mean standard deviation σ_{MEAN} was calculated from the error propagation equations as

$$\sigma_{\text{MEAN}} = \sqrt{\frac{\sigma_1^2 + \sigma_2^2 + \dots + \sigma_n^2}{n}}, \quad (5)$$

where σ_n is the standard deviation of the reflectance value of the n 'th sample.

In terms of the raw reflectance, the measurements presented in this paper can be compared with the measurements at the wavelength of 12.98 nm conducted in Laser-Laboratorium Göttingen e.V.¹¹ using a laser-produced plasma from a gas puff target. For the angle of $\theta_i = 80$ deg and $\theta_i = \theta_s$, the reflectance measured in our setup is at the level of $\sim 1.3 \times 10^{-3}$, which is very similar to the results presented in Ref. 11. For the angle of 45 deg, the data discussed in Ref. 11 for 12.98 nm represented the noise level of the detector, therefore there is no more data to continue the comparison. Our raw-reflectance measurements can be also compared with the results presented in Ref. 12. The reflectance of the Acktar Magic Black™

coating reported in our paper for the incidence angle of 18 deg is several times lower compared to the reflectance of the Acktar Spectral Black™ coating for near-normal incidence. However, it is comparable to the reflectance of the carbon-nanotube and carbon-foam coatings, which were presented as the lowest-reflectance cases in Ref. 12. A more rigorous measurement-geometry-independent comparison of our measurements for ~ 121.6 nm with measurements available in the literature for other wavelengths requires conversion of the raw reflectance into the BRDF, which is discussed below.

4 Phenomenological Model of the BRDF: Methodology

The measurements described in Secs. 2 and 3 were aimed at the raw reflectance of the Acktar Magic Black™ coating defined as a ratio of the sample-scattered signal intensity registered by the CCD camera to the reference intensity, measured with the beam illuminating the camera directly. The measurements were corrected for the background identified outside of the nominal light spot in the images captured by the camera. In this section, we discuss the process of conversion of the raw-reflectance measurements into the BRDF and the general approach to fitting a phenomenological model of the BRDF.

4.1 BRDF Function

The raw measurements of the reflectance discussed in Sec. 3 correspond to the ratio dP_s/P_i of the scattered power dP_s (in photons/s or W units) detected by the camera to the incident power P_i , so they depend on the geometry of the experimental setup, in particular on the diameter d of the aperture in front of the CCD camera and the aperture-sample distance r . A geometry-independent characterization of the reflectance properties of a surface is possible by using the BRDF defined as

$$\text{BRDF}(\theta_i, \varphi_i, \theta_s, \varphi_s) = \frac{dP_s}{P_i d\Omega_s \cos(\theta_s)}, \quad (6)$$

where $d\Omega_s$ is the solid angle subtended by the detector aperture and $\cos(\theta_s)$ accounts for Lambert-cosine's-law effects as proposed in Ref. 18. It can be shown that $\text{BRDF} = dL_s/E_i$ is the ratio of the radiance dL_s in a given scattering direction and the incident irradiance E_i . The unit of the BRDF is sr^{-1} .

In Fig. 7, we show the geometry convention. In the most general case, the BRDF is a function of the incidence direction (θ_i, φ_i) and the scattering direction (θ_s, φ_s) .

If the azimuthal angles φ_i and φ_s are measured from the specular plane, we have always $\varphi_i = 0$ (by the definition of our frame), and the dependence on φ_i can be omitted. Hence, only three angles are needed, and $\text{BRDF} = \text{BRDF}(\theta_i, \theta_s, \varphi_s)$. If only the specular plane is of interest, a convention $\text{BRDF} = \text{BRDF}(\theta_i, \theta_s)$ is used in the literature, where to distinguish between the

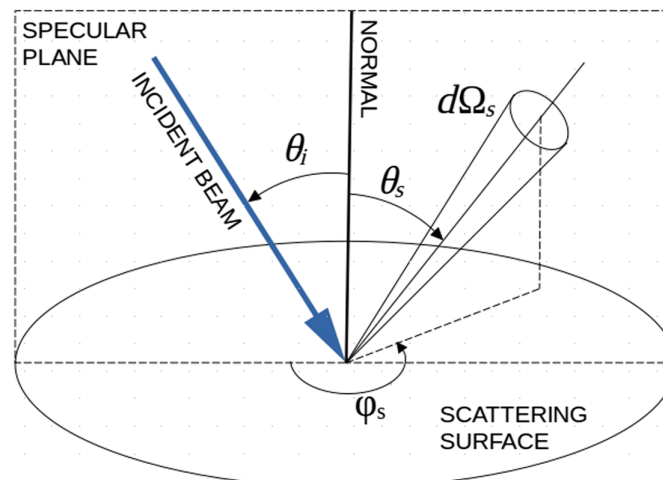


Fig. 7 Geometry convention used in this paper.

forward-scattering and backward-scattering parts, θ_s may take both positive and negative values. In our paper, $\theta_s > 0$ deg corresponds to the forward-scattering case ($\varphi_s = 180$ deg) and $\theta_s < 0$ deg corresponds to the backward-scattering case ($\varphi_s = 0$ deg).

4.2 Fitting Procedure

Challenges and complications related to the UV regime limit the number of reflectance measurements that can be collected in practice, which makes it difficult to obtain a dense coverage of the BRDF behavior as a function of θ_i and θ_s angles. For this reason, we use an approach described below, where fitting a function to the direct measurements allows us to characterize the BRDF behavior globally for ~ 121.6 nm. First, we use measurements of the BRDF available in the literature for 532 nm to find a simple closed-form function that can be used to fit the BRDF measurements for the Acktar Magic Black™ coating. We show that by using only selected measurement points in the fitting procedure, we can obtain a reasonable global fit to the measurements for 532 nm. This exercise for 532 nm is conceived as a test of the feasibility of obtaining a good global fit on a data set of the same sparseness as the measurements for ~ 121.6 nm. The same functional form that is shown to work properly for 532 nm is then used to fit the measurements for ~ 121.6 nm.

5 Phenomenological Model of the BRDF—Results

5.1 In-Specular-Plane Modeling for the VIS Range (532 nm)

There is a substantial amount of information available in the literature describing the BRDF for the Acktar Magic Black™ coating in the VIS of wavelengths, in particular for 532 nm. We use these data to pre-validate our approach and fix values of some fitting parameters that are used later for processing UV measurements.

First, we digitally extracted BRDF measurements from Figs. 2 and 3 in Ref. 7, which are shown as dashed lines in Fig. 8. The data describe the behavior of the BRDF in the specular plane. Then, we selected a subset S of the data containing a relatively small number of data points representing a similar set as the UV-range measurements described in Sec. 3. The data points from the subset S are shown as circles in Fig. 8. The measurements described in Ref. 7 do not cover the case $\theta_i = 75$ deg, thus, to make the VIS-range set more similar to the UV-range set from Sec. 3, we generated semi-synthetic data (shown as black circles in Fig. 8) for $\theta_i = 75$ deg by linear interpolation between the data sets for $\theta_i = 60$ deg (cyan dashed line) and $\theta_i = 80$ deg (magenta dashed line). The interpolation was done for $\ln(\text{BRDF})$, i.e., for the natural logarithm of the BRDF, which corresponds to the interpolation in the logarithmic scale.

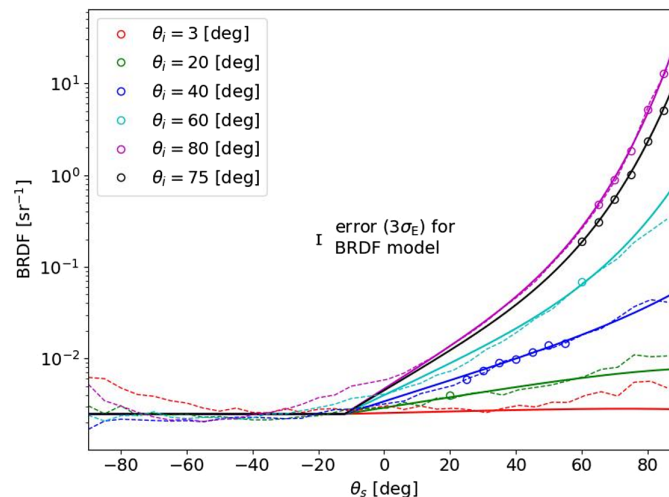


Fig. 8 BRDF measurement data for 532 nm (dashed lines), from which a limited subset S of data points (circles) was selected for pre-validation of fitting procedures used later for ~ 121.6 nm. The solid lines show the best globally fitted model for 532 nm. The error bar for the mean error $3\sigma_E$ of the fit is shown in the middle of the plot. Different colors represent different incidence angles.

A number of fitting functions were tested on the 532-nm data and finally, the following form:

$$\begin{aligned} \text{BRDF}(\theta_i, \theta_s) &= \text{BRDF}_0 \exp[a_1 \theta_i (\theta_s - \theta_{s0}) + a_2 \theta_i (\theta_s - \theta_{s0})^\alpha + a_3 \theta_i^2 (\theta_s - \theta_{s0})^\alpha] \quad \text{for } \theta_s \geq \theta_{s0}, \\ \text{BRDF}(\theta_i, \theta_s) &= \text{BRDF}_0 \quad \text{for } \theta_s < \theta_{s0}. \end{aligned} \quad (7)$$

was found to provide a reasonable global fit with a relatively small number of parameters BRDF_0 , α , θ_{s0} , a_1 , a_2 , a_3 . Note that since in this section, we consider only the variation of the BRDF in the specular plane, it is a function of the incidence angle θ_i and only one scattering angle θ_s . Note also that the angle θ_{s0} should not be confused with the specular angle. The angle θ_{s0} is simply defined as an angle measured in the specular plane below which the BRDF is constant in our BRDF model of Eq. (7). For fixed values of parameters α and θ_{s0} , the other parameters BRDF_0 , a_1 , a_2 , and a_3 can be found for $\ln(\text{BRDF})$ using the linear regression method as expansion coefficients in the functional space $[1, \theta_i (\theta_s - \theta_{s0}), \theta_i (\theta_s - \theta_{s0})^\alpha, \theta_i^2 (\theta_s - \theta_{s0})^\alpha]$. The linear regression method allows us to obtain a global fit, i.e., to fit measurements for different θ_i [i.e., all the pairs (θ_i, θ_s) represented by circles in Fig. 8] at once in one fitting step. Since the fitting procedure operates on $\ln(\text{BRDF})$, it minimizes the mean squared error in the logarithmic scale. To verify a posteriori the goodness of fit, we define the mean error

$$\sigma_E = \frac{1}{N_S} \sum |\ln(\text{BRDF}_{\text{fitted}}) - \ln(\text{BRDF}_{\text{measured}})|,$$

where the sum is computed over N_S data points in the subset S (i.e., over the circles in Fig. 8). Uncertainty propagation rules can be used to show that this error in the logarithmic scale can be considered as an approximation for the relative error

$$\sigma_{\text{RE}} = \frac{1}{N_S} \sum \frac{|\text{BRDF}_{\text{fitted}} - \text{BRDF}_{\text{measured}}|}{\text{BRDF}_{\text{measured}}}$$

of the BRDF itself in the linear scale.

This fitting step is then repeated for different values of the parameters α and θ_{s0} to find the minimum of the total relative error

$$\sigma_{\text{TRE}} = \frac{1}{N} \sum \frac{|\text{BRDF}_{\text{fitted}} - \text{BRDF}_{\text{measured}}|}{\text{BRDF}_{\text{measured}}},$$

where the sum is now computed over all of the N available data points for 532 nm (so over the dashed lines in Fig. 8, not only over the circles). In this approach, the parameters α and θ_{s0} can be referred to as hyperparameters (a term used in machine learning for higher-order parameters that are used as fixed in the ongoing step of fitting), and BRDF_0 , a_1 , a_2 , and a_3 are regular parameters obtained from the linear regression.

The best globally fitted model for 532 nm is shown by solid lines in Fig. 8. It was obtained for the following values of parameters: $\alpha = 4.5$, $\theta_{s0} = -12$ deg, $\text{BRDF}_0 = 2.49 \times 10^{-3}$ sr $^{-1}$, $a_1 = 6.57 \times 10^{-4}$ deg $^{-2}$, $a_2 = -2.90 \times 10^{-11}$ deg $^{-1-\alpha}$, and $a_3 = 9.76 \times 10^{-13}$ deg $^{-2-\alpha}$. The errors of the fit are as follows: $\sigma_E = 4\%$ and $\sigma_{\text{TRE}} = 12.9\%$. Using these parameter values in Eq. (7), we obtain a fit that provides an approximation of the behavior of the BRDF for 532 nm in the specular plane as a function of the incidence angle $0 \leq \theta_i \leq 90$ deg and the scattering angle $-90 \leq \theta_s \leq 90$ deg over ~ 4 orders of magnitude of the BRDF variability.

5.2 Modeling the BRDF in the Full Hemisphere for the VIS Range (532 nm)

The description of the BRDF behavior in the specular plane as discussed in Sec. 5.1 does not provide the full information needed for a general case of ray-tracing simulations or other computations aimed at estimating the radiation power scattered in an arbitrary direction. In general, the behavior out of the specular plane also needs to be known. For 532 nm, measurement data of this type are presented in Table 3 and Fig. 7 in Ref. 6. We use the data here to extend our model beyond the specular plane.

The BRDF presented in Fig. 8 is characterized by a strongly elevated forward-scattering side ($\theta_s \geq 0$ deg) and a flat backward-scattering side ($\theta_s < 0$ deg). Figure 7 in Ref. 6 shows that in the full hemisphere, the in-specular-plane profile of the BRDF spreads out of the specular plane, but the width of the spreading is different for different incidence angle θ_i . We try to capture this

Table 3 Comparison of TIS values obtained from the model presented in this paper with actual measurements.

	TIS			
	$\theta_i = 5$ deg	$\theta_i = 30$ deg	$\theta_i = 50$ deg	$\theta_i = 70$ deg
Measurements (Ref. 6)	0.8%	0.9%	1.4%	5.2%
Our model [Eqs. (7), (8), and (10)]	0.81%	1.09%	1.68%	4.0%

kind of behavior in our analytical model by defining BRDF^- and BRDF^+ as branches of the BRDF corresponding to $\theta_s < 0$ deg and $\theta_s \geq 0$ deg in the specular plane, respectively. A full-hemisphere dependence of the BRDF can be then obtained by using a weighted average:

$$\text{BRDF}(\theta_i, \theta, \varphi) = w\text{BRDF}^+ + (1 - w)\text{BRDF}^-, \quad (8)$$

where the weight

$$w = -\frac{|\varphi - 180|}{\Delta_\varphi} + 1 \quad \text{for } |\varphi - 180| < \Delta_\varphi$$

$$w = 0 \quad \text{for } |\varphi - 180| \geq \Delta_\varphi$$

is a piecewise-linear function of the azimuthal angle φ in the spherical coordinates. The weight w is conceived to take the value of 1 in the forward-scattering part ($\theta_s \geq 0$ deg, which corresponds to $\varphi = 180$ deg) of the specular plane, then to linearly decrease and take the value of 0 when the azimuthal distance $|\varphi - 180|$ from the forward-scattering part of the specular plane becomes larger than Δ_φ . In this formulation, a given direction in the scattering hemisphere is identified by the azimuthal angle $0 \leq \varphi < 360$ deg and the polar angle $0 \leq \theta \leq 90$ deg. For a given incidence angle θ_i and scattering direction (θ, φ) , using Eq. (7) and the best-fit parameters from Sec. 5.1, we can compute $\text{BRDF}^- = \text{BRDF}(\theta_i, \theta_s = -\theta)$, $\text{BRDF}^+ = \text{BRDF}(\theta_i, \theta_s = \theta)$, and the weight $w(\varphi)$. This allows us to finally compute $\text{BRDF}(\theta_i, \theta, \varphi)$ from Eq. (8). For the weight $w(\varphi)$, we need to know the value of the parameter Δ_φ , which determines the width (in the azimuthal angle φ domain) of the spread of the in-specular-plane profile in the out-of-specular-plane direction. To account for the dependence of the spread on θ_i seen in Fig. 7 in Ref. 6, we propose the following function: $\Delta_\varphi = c_1\theta_i + c_2$ (where $c_1 = -0.95$, $c_2 = 90.5$ deg), which gives isocontours in our Fig. 9 similar to those presented in Fig. 7 in Ref. 6.

Having a description of the BRDF in the full hemisphere, we can compute the total integrated scatter (TIS) as

$$\text{TIS}(\theta_i) = \iint \text{BRDF}(\theta_i, \theta, \varphi) \cos(\theta) \sin(\theta) d\theta d\varphi. \quad (9)$$

The quantity $0 \leq \text{TIS}(\theta_i) \leq 1$ tells us what fraction of the incident radiation power is scattered irrespective of the direction; in other words, $1 - \text{TIS}(\theta_i)$ is the fraction of the incident radiation power absorbed by the surface.

The BRDF measurements discussed in Refs. 6 and 7 display a folding (cf. Figs. 2 and 3 in Ref. 7 with our Fig. 8) at the highest values of the scattering angle θ_s , which has not been taken into account in our considerations so far. This folding is commonly interpreted as a spurious measurement effect, which appears when the forward scattering is measured very close to the surface. However, since the folding is present in real measurements, for direct comparison of TIS resulting from our BRDF model with Table 3 in Ref. 6, we need to include this effect. The effect affects only the forward-scattering branch, thus, we can introduce it as an additional modulation, which effectively works for the highest values of the scattering angle θ_s :

$$\text{BRDF}^+ = \frac{\text{BRDF}(\theta_i, \theta_s = \theta) \{1 - \text{erf}[a(\theta_s - \theta_{sf})]\}}{2}, \quad (10)$$

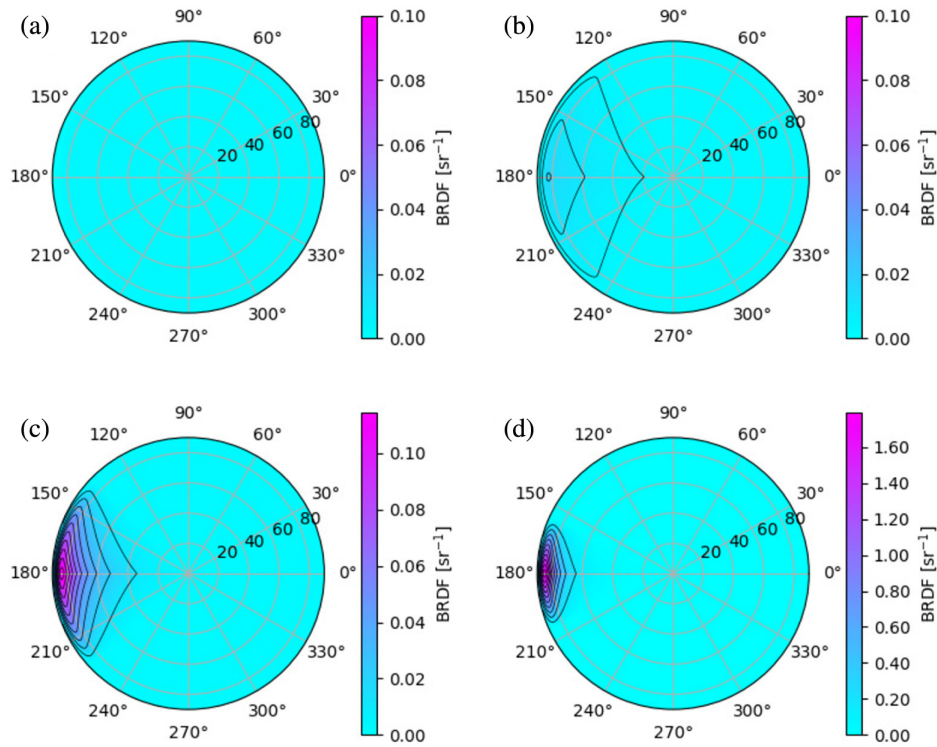


Fig. 9 Full-hemisphere dependence of the BRDF model of Eq. (8) for the incidence angles (a) $\theta_i = 5$ deg, (b) $\theta_i = 30$ deg, (c) $\theta_i = 50$ deg, and (d) $\theta_i = 70$ deg. A polar-plot convention is used (a kind of view from the top), where the radius represents the spherical-coordinates polar angle θ , and the angle around each plot represents the spherical-coordinates azimuthal angle φ . The color encodes the values of the BRDF as shown in the colorbars; additionally, some isocontours are overplotted. The plot was prepared to be directly comparable with Fig. 7 in Ref. 6. The only difference is that in our paper the left-side sector ($90 \leq \varphi \leq 270$ deg) represents the forward-scattering side, and the right-side sector is the backward-scattering part, whereas in Fig. 7 in Ref. 6 the backward-scattering and forward-scattering sides are defined in the opposite way.

where $a = 0.35 \text{ deg}^{-1}$ and $\theta_{sf} = 87 \text{ deg}$ are the parameters of the folding function, and $\text{erf}()$ is the Gauss error function. Figure 10(a) shows a comparison of the folded and unfolded BRDF dependence in the specular plane as included in our approach.

In Fig. 10(b), we also compare the maximum measured BRDF values from Refs. 6 and 7 with our model of Eq. (7) with folding by Eq. (10) included. Finally, the values of TIS presented in Table 3 in Ref. 6, i.e., scatterometer measurements in the full hemisphere for Acktar Magic Black™ coating, are compared in Table 3 with the integral of Eq. (9) for our full-hemisphere BRDF model of Eqs. (7), (8), and (10).

5.3 BRDF Model for the UV Range ($\sim 121.6 \text{ nm}$)

The approach, pre-validated in Secs. 5.1 and 5.2 on the 532-nm measurement data, is now applied to fit the reflectance measurements in the UV range described in Sec. 3. In the first step, Eq. (6) was applied to the raw-reflectance measurements from Tables 1 and 2 to obtain the corresponding BRDF values. For the experimental setup, the solid angle subtended by the camera aperture can be computed as $\Omega_s = 2\pi[1 - \cos(\rho)]$, where $\rho = d/(2r)$ is the angular radius of the spherical cap related to Ω_s . The diameter d of the aperture in front of the CCD camera and the aperture-sample distance r were slightly different in series I ($d = 7.2 \text{ mm}$, $r = 103.8 \text{ mm}$) of the measurements and series II ($d = 7.5 \text{ mm}$, $r = 110 \text{ mm}$), which is accounted for in the computations presented in this section.

In Fig. 11, we show the BRDF values (circles) computed from the raw-reflectance measurements presented in Tables 1 and 2. In series I, the reflectances for different samples were measured only for the specular angle. For this reason, the measurements are shown in Fig. 11 as a vertical series of circles at $\theta_i = \theta_s$ for $\theta_i = [18, 45, 75, 80] \text{ deg}$. Using the data points grouped by

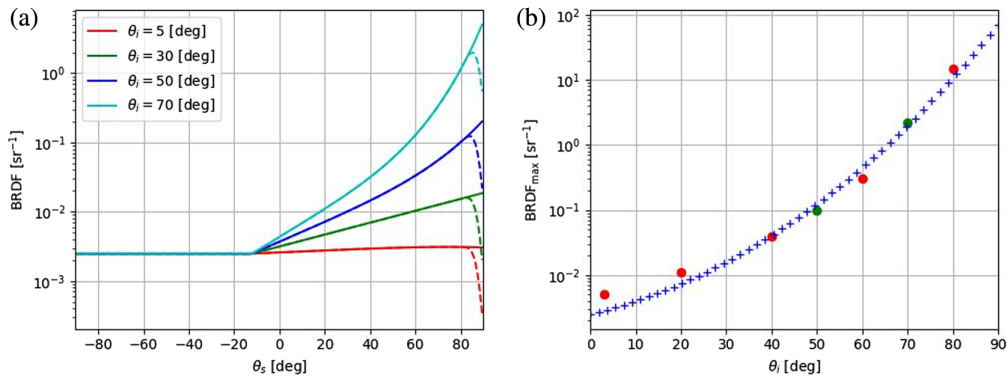


Fig. 10 (a) Illustration of the folding effect that appears in actual BRDF measurements for the highest values of the scattering angle θ_s . Solid lines show the unfolded BRDF, and dashed lines the BRDF folded using Eq. (10). (b) Dependence of the maximum BRDF value on the incidence angle. Red circles show the maximum measured values from Figs. 2 and 3 in Ref. 7, green circles show the maximum measured values from the bottom panels of Fig. 7 in Ref. 6, and blue crosses show the maximum values from our model in Eq. (7) with the folding by Eq. (10) included.

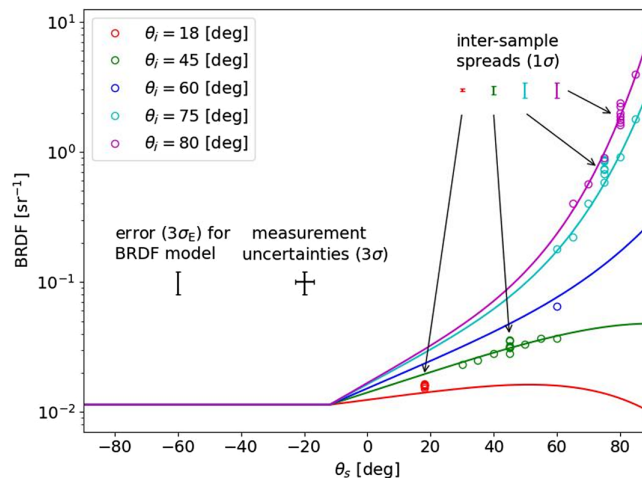


Fig. 11 Comparison of BRDF measurement data for the UV regime ~ 121.6 nm (circles) with the best globally fitted model (solid lines). The error bars for the mean error of the fit, measurement uncertainties, and inter-sample spreads are shown in the plot. Different colors represent different incidence angles.

the incidence angle θ_i , we computed inter-sample spreads (as the standard deviation) and plotted them in the form of 1σ error bars in Fig. 11, where the arrows connect a given spread with the corresponding group of data points. The measurement uncertainties estimated in Sec. 3 (the relative uncertainty of 6.5% for the reflectance, the absolute uncertainty of 1 deg for the angles θ_i and θ_s) are also shown in the form of 3σ error bars in the middle of the plot.

The reflectance measurements converted to the BRDF are then used as an input for the fitting procedure. The same functional form and hyperparameter values $\alpha = 4.5$ and $\theta_{s0} = -12$ deg are used as those found in Sec. 5.1 (i.e., from the best fit for 532 nm). Similarly to Sec. 5.1, the rest of the parameters of the fit are obtained from the linear regression method, where measurements for different θ_i , i.e., all (θ_i, θ_s) pairs represented by circles in Fig. 11, can be included in one global fit. The fitted parameter values for the UV regime (~ 121.6 nm) are $\text{BRDF}_0 = 1.14 \times 10^{-2} \text{ sr}^{-1}$, $a_1 = 4.02 \times 10^{-4} \text{ deg}^{-2}$, $a_2 = -6.9 \times 10^{-11} \text{ deg}^{-1-\alpha}$, and $a_3 = 1.34 \times 10^{-12} \text{ deg}^{-2-\alpha}$. The error of the fit is $\sigma_E = 6.4\%$. Using these parameter values in Eq. (7), we obtain a fit that provides an approximation for the behavior of the BRDF for ~ 121.6 nm in the specular plane as a function of the incidence angle $0 \leq \theta_i \leq 90$ deg and scattering angle $-90 \leq \theta_s \leq 90$ deg over ~ 3 orders of magnitude of the BRDF variability, as shown in Fig. 11.

One should note that an additional measurement for $\theta_i = \theta_s = 60$ deg (blue circle in Fig. 11) was not included in Tables 1 and 2. It was also not used in the fitting procedure described above. This measurement and the corresponding model curve (blue line) were added to Fig. 11 to verify if unseen-in-fitting measurements agree with the fitted model.

Currently, we have no access to out-of-specular-plane measurement data for ~ 121.6 nm, thus the only way of extending the model for the UV regime beyond the specular plane is by using the same formulation as discussed for 532 nm in Sec. 5.2. When computing BRDF⁺ and BRDF⁻, the best-fit-in-the-specular-plane parameter values given above in this section should be used, but for the rest of the procedure one should follow exactly the prescription given in Sec. 5.2. Due to strong similarities between the in-specular-plane BRDF for 532 and ~ 121.6 nm, this approach is considered as reasonable by the authors.

6 Validation by Ray Tracing Simulations

Since the main goal of this paper is to provide a prescription for the BRDF in the full hemisphere for a UV wavelength ~ 121.6 nm that can be used in computations, in this section, we present results of ray tracing simulations to show that the BRDF derived in Sec. 5 indeed gives similar raw reflectance as presented in Sec. 3.

The simulation is based on a simple forward ray tracing for the measurement setup for series II from Sec. 2. Figure 12 schematically shows the simulated setup.

A light source with a diameter of 0.5 mm is located 360 mm from the center of a sample of the size 40×40 mm². Three apertures A_1 - A_3 of diameters 4.8, 16, and 4.63 mm shaping the beam are placed at 32, 93, and 211 mm from the source, correspondingly. The apertures are centered at the optical axis between the centers of the source and the sample. The planes of the apertures are perpendicular to the axis. The beam from the source is divergent to make sure that the light spot at the last aperture is slightly larger than its diameter. The simulation neglects reflections/scattering from the planes containing the apertures, only rays within the apertures pass through further, and other rays are assumed to be perfectly absorbed. A consequence of this idealization is that effectively only the last aperture is important for the final shape of the beam in the simulations.

For the rays reaching the sample at a given incidence angle (set as a variable parameter in the simulation), the scattering angles are drawn from a three-dimensional probability distribution $p(\theta_i, \theta, \varphi)$, which is equal to a discretized integrand of TIS from Eq. (9), i.e.,

$$p(\theta_i, \theta, \varphi) = \text{BRDF}(\theta_i, \theta, \varphi) \cos(\theta) \sin(\theta) \Delta\theta \Delta\varphi.$$

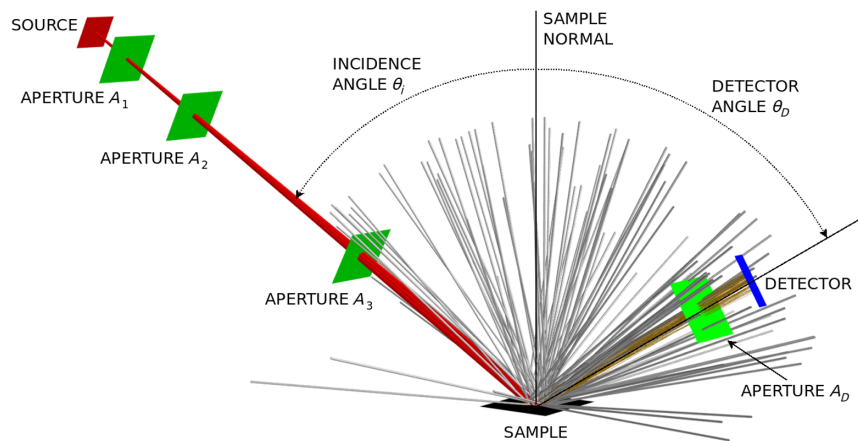


Fig. 12 Schematic view of the simulation setup. The incident beam (shown in red) is formed by three apertures A_1 - A_3 (green). Two types of rays scattered from the sample (black) are shown. Gray lines represent instances of rays scattered in random directions, and yellow lines show instances of scattered rays that were registered by the detector (blue). Between the sample and the detector, an additional aperture A_D is placed.

In practice, in our simulation, a three-dimensional discrete grid of $90 \times 90 \times 360$ points was used to span the probability dependence on θ_i , θ , φ . Drawing scattering directions from such a discrete grid leads to the appearance of some artificial patterns when small regions (in comparison with the probability-grid resolution of $1 \times 1 \times 1 \text{ deg}^3$) are of interest. To suppress the artificial patterns, we used an additional uniform-distribution-based randomization of the directions of scattered rays within each cell.

At a distance of 110 mm from the center of the sample along a given detector-related direction (θ_D, φ_D) , an aperture A_D with a diameter of 7.5 mm was placed, which subtended a small solid angle from the entire hemisphere in which the rays are scattered from the sample. Further, at a distance of 30 mm from the aperture, a rectangular detecting plane $25.6 \times 6.375 \text{ mm}^2$ was located. Rays traversing the plane were counted as detected.

In Fig. 13, the results of simulations for the incidence angle $\theta_i = 80 \text{ deg}$ and different detector angles are juxtaposed with CCD images registered in measurements discussed in Secs. 2 and 3. Simulations are noisier due to a higher Poisson noise caused by smaller count (ray) numbers, but a general agreement between the simulations and measurements is observed.

One can see several peculiarities in the measurements that are captured by the simulations. For example, there is a systematic evolution of the light spot from the top to the bottom panel (as the detector angle increases), where the boundaries of the light spot are strongly blurred in the top panel and sharper in the bottom panels. A regular gradient of the brightness of the light spot is seen, the left side being slightly brighter than the right side for the detector angles 65 deg to 80 deg. This gradient in the images is related to the steep gradient of the BRDF in the specular plane for large θ_i and θ_s values, as shown in Fig. 11. However, in the bottom panels (detector angle 85 deg), the gradient becomes reversed (right-hand side of the light spot is now brighter) with respect to the rest of the panels. At this angle, we are so close to the sample surface that the BRDF folding effect (discussed earlier and shown in the left panel of Fig. 10) kicks in. All these peculiarities are seen both in the measurement images and in the simulations.

Figure 14 shows a comparison of the measured and simulated raw reflectance for the entire series II of the measurements. The raw reflectance in the simulations was computed similarly as in the measurements, i.e., in the simulated images, a rectangle on the light spot [see Fig. 13(b)] was defined. The reflectance was computed as the ratio of the averages for the sample-scattered and reference images over the same rectangle. A general agreement between the measurements and simulations is observed in Fig. 14.

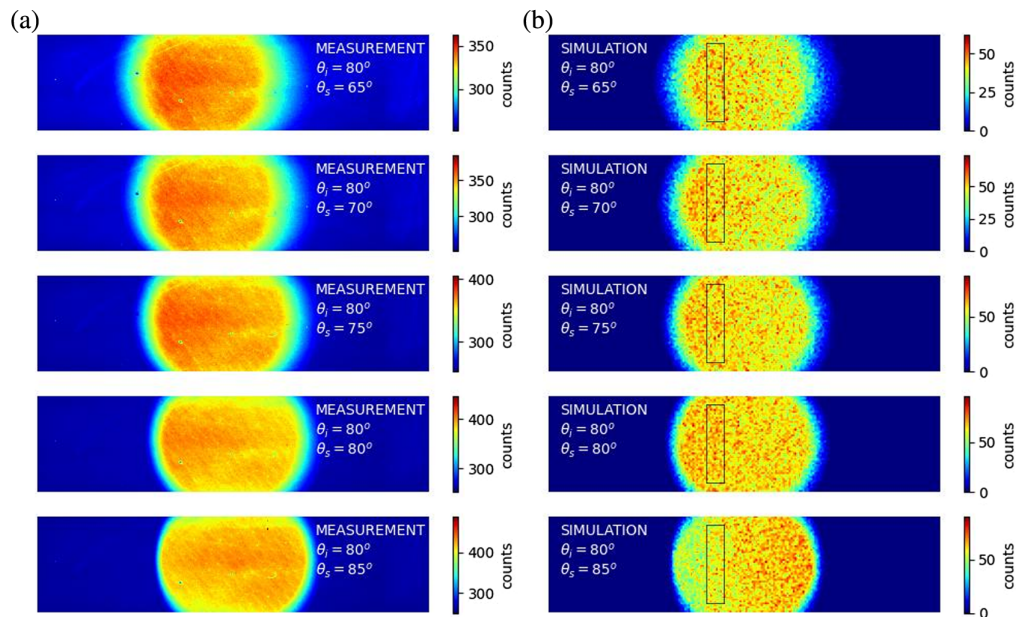


Fig. 13 Comparison of (a) measured CCD images registered in measurements discussed in Secs. 2 and 3 with (b) ray tracing simulations.

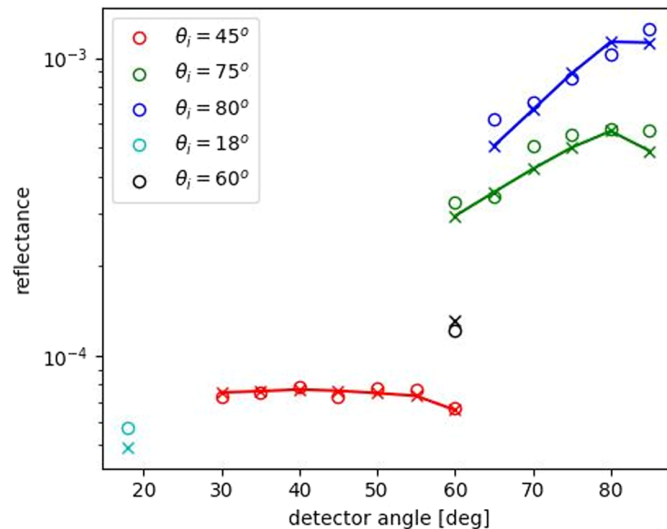


Fig. 14 Comparison of the measured (circles) and simulated (crosses) raw reflectance for series II of measurements in the UV regime discussed in Sec. 3. Different colors correspond to different incidence angles.

7 Discussion and Conclusions

This paper presents the results of reflectance measurements for the Acktar Magic Black™ coating in the UV regime around ~ 121.6 nm and the resulting BRDF function. A laser-plasma X-ray source based on the gas-puff target was used in combination with an Acton narrowband filter to generate radiation in a narrow range of wavelengths at the crossover between the FUV and EUV regimes. Six samples coated with Acktar Magic Black™ were studied in an optical setup with a back-illuminated CCD camera as the photon-flux measuring device. The measurements characterize comprehensively certain parts of the scattering hemisphere, including quasi-perpendicular (relative to the sample surface) and quasi-parallel cases. Tables 1 and 2 along with Figs. 4 and 6 summarize the raw reflectance measurements. Further in the paper, the measurements are shown to properly constrain the parameters of the derived phenomenological model of the BRDF.

Our methodology for the BRDF model was pre-validated in the VIS regime (532 nm), where a substantial body of data on the reflectance properties of the coating is available in the literature. Therefore, a BRDF model for 532 nm is also discussed here as a byproduct of our analyses for the UV regime. Fitted functions are demonstrated in Figs. 8 and 11 to provide a good approximation to the measurements, which is formally confirmed by small errors $\sigma_E = 4\%$ for the VIS regime and $\sigma_E = 6.4\%$ for the UV regime. An out-of-specular extension was proposed for the BRDF models based on measurement data for 532 nm available in the literature. Figure 9 and Table 3 in our paper show that the out-of-specular extension agrees with the measurements presented in Ref. 6. Therefore, a full-hemisphere BRDF model is proposed for both 532 and ~ 121.6 nm.

In Fig. 11, error bars for inter-sample spreads and measurement uncertainties were added to give the reader a glimpse of how the modeling error compares with other uncertainties. Note that the inter-sample spreads are shown as 1σ , whereas the other errors are shown as 3σ , thus our study suggests that the inter-sample variability of the reflectance is the largest source of uncertainty for the grazing scattering (i.e., $\theta_i > 60$ deg).

In the numerical simulations presented in Sec. 6, the BRDF model for ~ 121.6 nm was used to verify if the raw-reflectance measurements from Sec. 3 were correctly reproduced. This simulation also included images of the light spot created on an imaging detector. The simulations and measurements are in agreement, including certain peculiarities discussed in Sec. 6.

Taking into account the character of the variability of the BRDF for the coating under consideration, the values of the parameter BRDF_0 [see Eq. (7)] can be used to get a rough estimate of the TIS for the perpendicular incidence. It is possible because for small incidence angles, the BRDF dependence on the scattering angle is relatively flat (see Figs. 8 and 11) and can be approximated by the Lambertian-scattering model (the same scattering probability in each

direction) with $\text{BRDF} = \text{TIS}/\pi = \text{const}$. Therefore, a rough estimation of $\text{TIS} = \pi \text{BRDF}_0$ gives $\sim 0.8\%$ for 532 nm and $\sim 3.6\%$ for ~ 121.6 nm, which suggests a much higher reflection (or much lower absorption) of the UV radiation as compared to the VIS for the perpendicular incidence. For higher values of the incidence angle, the Lambertian-scattering model does not apply and the full dependence of the BRDF on the scattering angle must be considered. For $\theta_i = 70$ deg, we obtained a TIS estimation of $\sim 5.8\%$ for ~ 121.6 nm, which is comparable with 5.2% obtained in the measurements for 532 nm (see Table 3). Therefore, the Acktar Magic Black™ seems to absorb less UV than VIS radiation, but only for the perpendicular incidence, whereas for higher incidence angles the absorption becomes comparable to that in the VIS range. This can be easily explained if we look at the maximum values in Figs. 2 and 5 and the plateau (corresponding to BRDF_0) in the two plots. For the UV regime, the plateau is higher than for the VIS regime, but the maximum value (for the largest incidence and scattering angles) is lower in UV in comparison with VIS. In general, the results obtained in this paper agree with other publications, where the scattering of light from Acktar coatings was studied.^{19–22}

It is known that the morphology of a given surface is crucial for the absorption and scattering of light. The surface of coatings manufactured by Acktar can be described as cauliflower-surface-like morphology (see, e.g., Fig. 6 in Ref. 19) with irregular curds at many scales. Such structures may be expected to effectively scatter and trap photons in multiple-reflection configurations, which increases the probability of the absorption of light. This type of surface morphology can also strongly reduce the probability of backward scattering of light for small incidence angles. Microscopic mechanisms determining the absorbing properties of coatings are beyond the scope of our paper. However, such theoretical studies explaining the role of the surface morphology can be found elsewhere, e.g., in Ref. 23. The simulations were performed for different idealized models of surface roughness including V-type grooves, sinusoidal structure, and randomly distributed surface irregularities. This theoretical study suggests that for these types of surface morphology, the absorption ratio generally decreases with the incidence angle, which means that the reflectance characterized by the BRDF and TIS can be expected to increase. The results obtained in our paper (low normal-incidence reflection, higher grazing-incidence reflection) are qualitatively consistent with the theoretical results reported in Ref. 23.

The form of the fitting function in Eq. (7) assumes that for $\theta_s < \theta_{s0}$, the BRDF curves for different θ_i merge, but, apparently, more flexibility for $\theta_s < \theta_{s0}$ could lead to a better fit between the 532-nm measurements (represented by dashed lines) and the BRDF model (solid lines) in Fig. 8. However, one should bear in mind that the model is fitted to a subset S of the points represented by the dashed lines. Therefore, the model must have significant rigidity, which is ensured by its functional form if a relatively sparse set of measurements is to be fitted.

In summary, we provide a full-hemisphere characterization of the reflectance properties of the Acktar Magic Black™ coating for ~ 121.6 and ~ 532 nm as BRDF models fitted to actual measurements. The models are given as closed-form expressions, thus they can be used in manual estimates and incorporated into all kinds of ray-tracing software, including customized ray-tracing computations implemented from scratch or commercial software like, e.g., Zemax or FRED. The model for ~ 121.6 nm is conceived to fill a gap in the literature, regarding the characterization of reflectance of the Acktar Magic Black™ coating in the proximity of the Lyman- α spectral line for hydrogen, which is of interest in satellite-instrument applications as the brightest spectral line in the solar spectrum in the UV range. It is important to emphasize the critical role of the raw-reflectance measurements discussed in Secs. 2 and 3, as constraining the parameters of the BRDF model derived for ~ 121.6 nm. As shown in Fig. 14, simulations based on the proposed BRDF model are in full agreement with the raw-reflectance measurements, which cross-validates the measurement and modeling aspects of our work.

Disclosures

The authors have no relevant financial interests in the manuscript and no other potential conflicts of interest to disclose.

Code and Data Availability

Reflectance measurement data used in this work are listed in Tables 1 and 2.

Acknowledgments

The results reported in this paper were obtained within a collaborative project between the Military University of Technology (WAT) and the Space Research Centre of the Polish Academy of Sciences (CBK PAN). The work at CBK PAN was supported by Polish Ministry for Education and Science under Contract No. MEiN/2021/2/DIR. The research at MUT was supported by the National Science Center Project No. 2020/39//ST7/03194. Martyna Wardzińska would like to express her deepest appreciation to the PADReS team at the FERMI free electron laser for the valuable experience in the field of VUV optics, which was helpful during the writing of this article. The staff-exchange visit to FERMI FEL was funded by the Laserlab Europe project (Grant Agreement ID: 871124).

References

1. Y.-C. Kim, P. De Bisschop, and G. Vandenberghe, “Evaluation of stray light and quantitative analysis of its impact on lithography,” *J. Micro/Nanolith. MEMS MOEMS* **4**(4), 043002 (2005).
2. J. A. R. Samson and D. L. Ederer, Eds., *Vacuum Ultraviolet Spectroscopy*, Elsevier (2000).
3. D. J. McComas et al., “Interstellar mapping and acceleration probe (IMAP): a new NASA mission,” *Space Sci. Rev.* **214**, 116 (2018).
4. S. Tarnopolski and M. Bzowski, “Neutral interstellar hydrogen in the inner heliosphere under the influence of wavelength-dependent solar radiation pressure,” *Astron. Astrophys.* **493**, 207–216 (2009).
5. Acktar Company, “Magic Black™ coating,” 2024, <https://acktar.com/product/magic-black/>.
6. M. Romoli et al., “METIS: the visible and UV coronagraph for solar orbiter,” *Proc. SPIE* **10563**, 105631M (2017).
7. J. Y. Plesseria et al., “Utilisation of Acktar Black coatings in space applications,” in *Int. Symp. on Mater. in the Space Environ. (ISMSE)* (2018).
8. S. Ben-Ami et al., “The scientific payload of the Ultraviolet Transient Astronomy Satellite (ULTRASAT),” *Proc. SPIE* **12181**, 1218105 (2022).
9. J. P. Gardner et al., “The James Webb Space Telescope,” *Space Sci. Rev.* **123**, 485–606 (2006).
10. O. Grasset et al., “Jupiter ICy moons Explorer (JUICE): an ESA mission to orbit Ganymede and to characterise the Jupiter system,” *Planet. Space Sci.* **78**, 1–21 (2013).
11. S. Doring and K. Mann, “EUV reflectivity measurements on Acktar sample magic black,” https://acktar.com/wp-content/uploads/2017/12/Low_reflectance_at_Extreme_Ultraviolet_EUV.pdf.
12. S. R. McCandliss et al., “Scattered light characterization of FORTIS,” *Proc. SPIE* **10397**, 1039718 (2017).
13. ISO International Standard 21348: 2017, *Space Environment (Natural and Artificial) – Process for Determining Solar Irradiances*, International Standards Organization (2007).
14. H. Fiedorowicz et al., “Strong extreme ultraviolet emission from a double-stream xenon/helium gas puff target irradiated with a Nd:YAG laser,” *Opt. Commun.* **184**, 161–167 (2000).
15. Acton Company, “Products: VUV/UV narrowband filters,” 2024, <https://www.actonoptics.com/products/filters-narrowband>.
16. A. Bartnik et al., “Low temperature photoionized Ne plasmas induced by laser-plasma EUV sources,” *Laser Part. Beams* **33**(2), 193–200 (2015).
17. B. Dean and W. J. Dixon, “Simplified statistics for small numbers of observations,” *Anal. Chem.* **23**(4), 636–638 (1951).
18. F. E. Nicodemus et al., *Geometrical Considerations and Nomenclature for Reflectance*, National Bureau of Standards, Washington DC, Washington (1977).
19. Y. Salomon et al., “Qualification of Acktar black coatings for space application,” in *Proc. Int. Symp. on Mater. in a Space Environ.*, Aix-En-Provence, France (2009).
20. M. Hauptvogel et al., “Light scattering characterization of optical components for space applications,” *Proc. SPIE* **10562**, 1056213 (2017).
21. A. Yevtushenko et al., “Vane-free design for star trackers and telescopes,” *Proc. SPIE* **10562**, 1056215 (2017).
22. A. Yevtushenko et al., “New light absorbing material for grazing angles,” *Proc. SPIE* **11180**, 111808D (2019).
23. C. Niu et al., “Influence of surface morphology on absorptivity of light-absorbing materials,” *Int. J. Photoenergy* **2019**, 1476217 (2019).

Marek Strumik is a research scientist at the Space Research Centre of the Polish Academy of Sciences, where he received his PhD in physics in 2006 after receiving his MS degree in physics from Gdansk University of Technology in 2002. He is the leading author or co-author of more than 30 peer-reviewed journal papers. His current interests include satellite UV instrumentation techniques and numerical methods for modeling and analysis of satellite measurements/observations.

Martyna Wardzińska is an engineer and doctoral candidate at the Military University of Technology. She received her BS degree in space engineering in 2020 and her MS degree in optoelectronics in 2021. Her current research interests include X-ray and VUV optics, design and simulation of free-electron-laser beamlines, X-ray, and VUV astronomical optics.

Przemysław Wachulak received his PhD in electrical and computer engineering from Colorado State University, USA, in 2008, habilitation degree in physics in 2013 from the University of Warsaw, and full professorship in 2018. Currently, he is a professor at the Military University of Technology in Poland. He is the author and co-author of more than 250 peer-reviewed journal papers. His works on new EUV/SXR laser-plasma sources for nanoimaging, holography, NEXAFS, OCT, metrology, and radiobiology.

Biographies of the other authors are not available.